Research Article | Vol. 12, No. 1 / 1 January 2021 / Biomedical Optics Express 173
Biomedical Optics EXPRESS

Hyperspectral microscopy combined with DAPI staining for the identification of hepatic carcinoma cells

KUNXING LIU,[1,2] SIFAN LIN,[1,2] SIQI ZHU,[1,2,3,*] YAO CHEN,[1,2] HAO YIN,[1,2] ZHEN LI,[1,2,3] AND ZHENQIANG CHEN[1,2,3]

[1]*Guangdong Provincial Engineering Research Center of Crystal and Laser Technology, Guangzhou 510632, China*
[2]*Department of Optoelectronic Engineering, Jinan University, Guangzhou 510632, China*
[3]*Guangdong Provincial Key Laboratory of Optical Fiber Sensing and Communications, Guangzhou 510632, China*
[*]*tzhusiqi@jnu.edu.cn*

Abstract: In this study, the DAPI staining is firstly reported for use in the identification of hepatic carcinoma cells based on hyperspectral microscopy. Nuclei in cancer cells usually contain more aneuploidies than that in normal cells, leading to the change of DNA content. Here, we stain hepatic carcinoma tissues and normal hepatic tissues with 4',6-diamidino-2-phenylindole (DAPI) which is sensitive to the DNA content as a fluorochrome binds to DNA. Consequently, the difference in DNA content between hepatic carcinoma cells and normal hepatic cells can be identified by the fluorescent spectral characteristics. Harnessing the hyperspectral microscopy, we find that the fluorescent properties of these two kinds of cells are different not only in the intensity but also in the spectral shape. These properties are exploited to train a support vector machine (SVM) model for classifying cells. The results show that the sensitivity and specificity for the identification of 1000 hepatic carcinoma samples are 99.3% and 99.1%, respectively.

1. Introduction

4′,6-diamidino-2-phenylindole (DAPI) is one of the classical DNA-specific fluorochromes that binds strongly to adenine–thymine rich regions of DNA [1]. The absorption peaks of DAPI locate at 222 nm, 259 nm, and 340 nm. Normally, a mercury lamp is used in combination with a commercial bandpass filter to produce the light around ~340 nm for matching the absorption peak of DAPI. The fluorescence of free dye of DAPI is weak with an emission peak at ~453 nm; while binds to DNA, the fluorescence quantum yield increases significantly [2]. So, the DNA content can easily be reflected by the fluorescent intensity when samples are stained with DAPI. Since DAPI was first suggested for use in flow cytometry by W. Göhde et al. [3], the flow cytometry examination has become one of the most effective ways for the cellular DNA content/ploidy type detection [2,4–6] and been widely used for the tumor study and diagnosis [7–11]. Especially, the cell analysis speed and the cell separation speed of the flow cytometer are extremely high.

Gross chromatin imbalance is a well-recognized feature of various kinds of cancers in human body [12], which means the cancer tissues often contain much more aneuploidies than the normal tissues. Therefore, the flow cytometry examination with DAPI staining can be utilized for the pre-diagnosis of tumor by counting the frequency of aneuploidy of cell population. In this method, the DNA content is estimated by the fluorescent intensity. However, the fluorescent intensity detection is susceptible to experiment conditions, such as test equipment, excited source, temperature, and storage time of samples, even a small change of experiment conditions will lead to the change of the estimated result. To improve the accuracy and applicability of the cancer cell identification, more fluorescent features, such as spectral features and spatial features are

#412158 https://doi.org/10.1364/BOE.412158
Journal © 2021 Received 19 Oct 2020; revised 29 Nov 2020; accepted 30 Nov 2020; published 8 Dec 2020

Biomedical Optics EXPRESS

required. Considering the flow cytometry only can obtain the average fluorescent intensity of the sample and the flow cytometry examination requires a relatively complicate pretreatment process for the sample, we replace it with a hyperspectral microscopy in this study.

Hyperspectral imaging (HSI) technology can both obtain the spatial and spectral information of samples, which enables the analysis of each pixel in the field of view (FOV). HSI technology has already been employed to identify various kinds of cancer cells [13–17]. Almost all relevant samples used in these studies are stained with hematoxylin–eosin (HE). As a pH-sensitive dye, hematoxylin–eosin can reveal the difference in nuclear pH value of cancer and normal cells via their spectral characteristics [18,19]. Yet, the change of pH value of nuclei in cancer cells is quite small, leading to the relatively low specificity of identification. Moreover, the eosin for cytoplasm staining is not necessary and even has a bad effect on the extraction of target nuclei and their spectra. Compare with the HE stain, the DNA-specific stain of DAPI can depress the noise from background significantly and is more sensitive to the variation in nucleic acid. In this study, a hyperspectral microscopy is firstly used to analyze the spectral characteristics of hepatic carcinoma and normal hepatic cells stained with DAPI. We find that the DAPI-DNA complex owns two emission centers. The blue emission is strong and has been widely reported by former researches; while the red emission is very weak and barely observed. These two emissions react differently to the DNA content, so the change of DNA content affects not only the fluorescent intensity but also the spectral shape. In this study, we used the spectra to train a support vector machine (SVM) model for the identification. The results showed that the sensitivity and specificity of the identification for 1000 hepatic carcinoma samples were 99.3% and 99.1%, respectively.

2. System and samples

2.1. Hyperspectral microscopy

The hyperspectral microscopic system used in our experiment is shown as Fig. 1(a). The Xenon lamp with a narrow bandpass UV filter is used to generate the exciting light at 360 nm. When this light enters the inverted microscope (ECLIPSE T_i-U, Nikon), it is focused onto the sample by an infinity -corrected microscope objective lens and excites the fluorescence of the sample. Then, the fluorescence passes through the dichroic mirror, the liquid crystal tunable filter (LCTF) (VariSpecVIS, CRI Inc.), and is finally captured by the CMOS camera (ORCA-Flash 4.0 LT C11440-42U, HAMAMATSU). The long pass dichroic mirror with a cut-off wavelength at 405 nm is used to separate the exciting light and the fluorescence, and the LCTF is used to realize the single–wavelength imaging. By changing the voltage of the LCTF continually, we can collect a series of single–wavelength images over the entire spectral range of 450–720 nm with a spectral resolution of 2 nm. These images can form a spectral cube (Fig. 1(b)) so that we can obtain the spectral information of each pixel in the image.

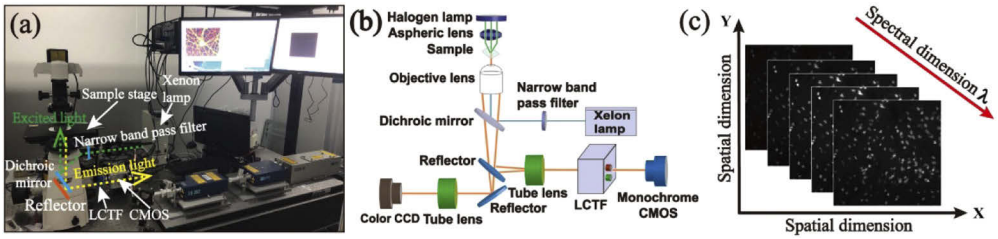

Fig. 1. Hyperspectral microscopy. (a) is hyperspectral experimental system. (b) is the optical diagram of the system. (c) is the hyperspectral cube, which presents the two-dimensional spatial information and one-dimensional spectral information of the sample.

Biomedical Optics EXPRESS

2.2. Samples

Slide samples of 20 cases of hepatic carcinomas were retrieved for this study. The morphologic characteristics of nuclei in the slide samples (Fig. 2(c) and Fig. 2(d)) were firstly examined by microscopy, and the grades of the hepatic carcinoma cells were classified based on the World Health Organization (WHO) criteria. Results demonstrated that most of the hepatic carcinoma cells in the slides are moderately differentiated (G2) or poorly differentiated (G3). In addition, slide samples of 20 cases of normal hepatic tissues (Fig. 2(a) and Fig. 2(b)) were also retrieved for this study. All samples were fixed by formalin, stained with DAPI and stored at 2°C. The thicknesses of these samples are about 5 µm. The hepatic carcinoma slide samples were extracted from different persons, as well as the normal hepatic slide samples. All these samples are provided by Bioaitech Co., Ltd.

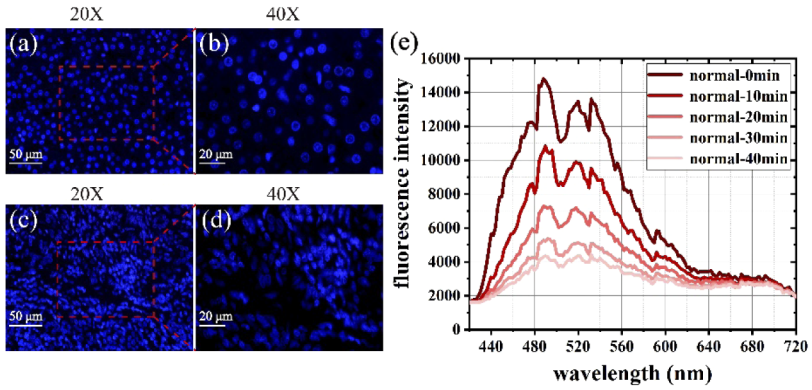

Fig. 2. The images of DAPI-stained samples and the effect of photobleaching of DAPI-stained samples. (a) and (b) are images of normal hepatic cells captured by the 20X (N. A. = 0.5) and 40X (N. A. = 0.5) objective lens, respectively. (c) and (d) are the images of hepatic carcinoma cells captured by the 20X and 40X objective lens, respectively. (e) is the photobleaching of DAPI-stained normal cells at different photobleaching time.

The fluorescence of the DAPI-stained sample is easy to be bleached by the strong exciting light. According to our experimental result, the fluorescence barely decreased during the wavelength-scanning of 450 nm-720 nm (about 40 seconds). However, it decreased by ~25% after ten minutes (Fig. 2(e)) and cannot restore its original status by keeping the sample in a dark environment for hours. Therefore, we recorded the spectra at different time. The first scanned data is used for the identification and all scanned data are used for the investigation of photobleaching.

3. Method and results

3.1. Spectra acquisition and analysis

We scanned every slide sample and obtained 40 spectral cubes corresponding to the range of 450–720 nm and the spectral resolution of 2 nm. To select the field of view (ROV) properly, a 20X objective (N. A. = 0.5) was used to capture the hyperspectral images and we chose the region around cancer nests in the slide sample. As shown in Fig. 3, cancer nest is a mass of cancer cells expanding from a common center. The distinct border between the normal tissue and the cancer nest can help us to find cancer cells and extract the fluorescent spectra of their nuclei with precisely.

1000 fluorescent spectra of normal nuclei and 1000 fluorescent spectra of cancer nuclei were extracted from 40 spectral cubes respectively for the analysis. The spectra of normal cells were

Biomedical Optics EXPRESS

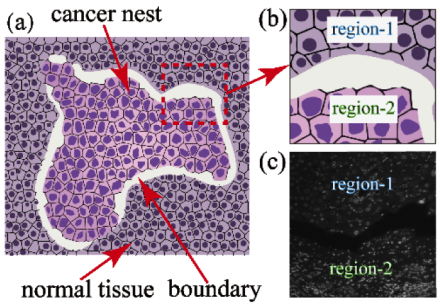

Fig. 3. Cancer nest in the tissue slide. (a) is the schematic diagram of cancer nest in the tissue slide. (b) shows the border of cancer nest. Region 1 and region 2 are the normal tissue and the cancer nest, respectively. (c) is the image of the border of cancer nest. Region 1 and region 2 are the normal tissue and the cancer nest, respectively.

extracted from slides of normal tissues, while the spectra of cancer cells were extracted from slides of hepatic carcinomas. The spectra were extracted from each selected pixel, and the target pixels in the train group were selected manually. Just in case, more situations should be taken into consideration, we not only extracted spectra from different nuclei but also extracted spectra from different points in the same nucleus. Especially, all selected spectra of cancer nuclei were preidentified by the pathological morphology examination.

The average spectral cures of normal and cancer nuclei with the fluctuation of individuals were illustrated as Fig. 4(a). One can see that the fluorescent intensity of the cancer nucleus is much higher than that of the normal cell. This is caused by the high DNA content of the cancer nucleus, which is in accordance with former studies [20–22]. Besides, the normalized average spectral cures with the fluctuation of individuals (Fig. 4(b)) demonstrates that there is a small difference in the spectral shapes between normal and cancer nuclei, especially at the long–wavelength (>560 nm) region.

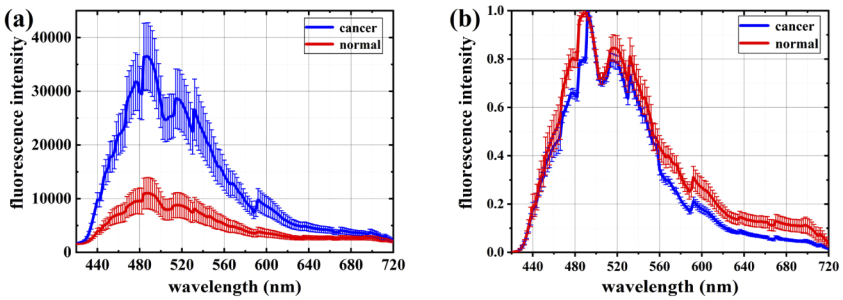

Fig. 4. Fluorescent spectra of normal and cancer nuclei stained with DAPI. (a) is the average spectral cures with the fluctuation of individuals. (b) is the normalized spectral cures with the fluctuation of individuals.

Further, we excited the sample continually and recorded the fluorescent spectra of a certain point every ten minutes, so we can observe the photobleaching process of the DAPI-stained sample. As shown in Fig. 5, the normalized spectra at different time do not overlap at the long–wavelength region, and a red emission peak became significant with the increasing exciting time. It means the DAPI-DNA complex owns two emission centers and their bleaching speeds are different.

According to the results shown as Fig. 4(a), the high DNA content in the cancer nucleus can lead to the enhancement of both emissions. Yet, the enhancement effects for the blue emission

Biomedical Optics EXPRESS

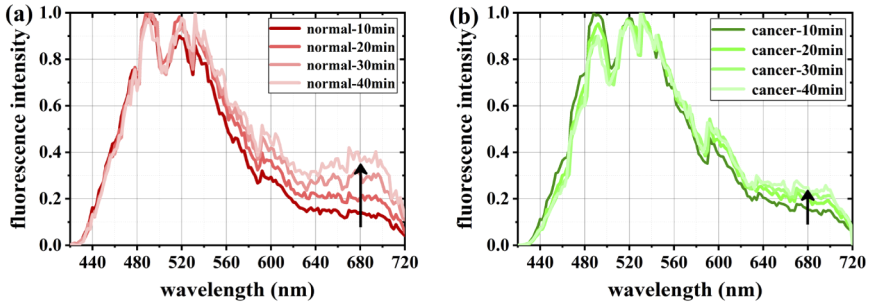

Fig. 5. The change of the fluorescence of normal cells (a) and cancer cells (b) with the increasing exciting time.

and the red emission are different. This is the reason why the spectral shape of the cancer nucleus is different from that of the normal nucleus (Fig. 4(b)).

3.2. Model training and testing

Since the spectral features can reveal the difference in DNA content, a training group formed with 1000 fluorescent spectra of normal nuclei and 1000 fluorescent spectra of preidentified cancer nuclei was used to train a support vector machine (SVM) model for the cell identification. Moreover, a testing group formed with 1000 fluorescent spectra of normal nuclei and1000 fluorescent spectra of cancer nuclei was employed to evaluate the SVM model. Especially, there is no overlap of the data between the training group and the testing group.

Figure 6 demonstrates the sensitivity (SEN), specificity (SPEC) as a function of the amount of training samples. SEN is a measure of the proportion of positives identified correctly in all positives, SPEC is a measure of the proportion of negatives identified correctly in all negatives. Besides, we also use the positive precision (P_{pr}) to evaluate the identification. P_{pr} is a measure of the proportion of positives identified correctly in all samples identified as positives. In this study, the cancer cells are the positive samples, and these parameters are defined by the formulas shown below [23]:

$$SEN = \frac{TP}{TP + FN} \tag{1}$$

$$SPEC = \frac{TN}{TN + FP} \tag{2}$$

$$P_{pr} = \frac{TP}{TP + FP} \tag{3}$$

where *TP* and *TN* present the number of true positives and the number of true negatives, while *FN* and *FP* present the number of false negatives and the number of false positives, respectively.

The training group that contains 2000 samples is large enough for the model training because the SEN and SPEC both become stable when the amount of training samples is higher than 300. The corresponding results of the identification are shown in Table 1.

Table 1. Classification results obtained using SVM model based on original spectra

Actual	normal	cancer
normal	991	9
cancer	7	993

The SEN, SPEC, P_{pr} for cancer cells were 99.3%, 99.1% and 99.1%, respectively. The high accuracy rate of the identification is caused by the significant difference in the fluorescent intensity

Biomedical Optics EXPRESS

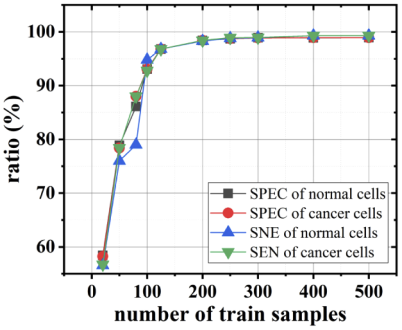

Fig. 6. The sensitivity and specificity of normal cells and cancer cells as functions of the number of training samples. In all cases, half of the training samples are the spectra of normal nuclei and the rest are the spectra of cancer nuclei.

between normal and cancer nuclei, shown as Fig. 4(a). However, the fluorescent intensity is susceptible to experiment conditions. Once the experiment conditions change, the accuracy rate may decrease significantly.

Considering the spectral shape can also reveal the DNA content, we used the normalized fluorescent spectra to train the SVM model. The normalization for spectra can remove the difference in fluorescent intensity so that the performance of the identification mainly depends on the difference in spectral shape. We used the same testing group mentioned above to evaluate the new model and the results are shown in Table 2.

Table 2. Classification results obtained using SVM model based on normalized spectra

Actual	normal	cancer
normal	989	11
cancer	8	992

Obviously, the new model can also identify normal and cancer cells precisely (SEN = 99.2%, SPEC = 98.9% and P_{pr}=98.9%), even the difference in fluorescent intensity between normal and cancer nuclei are not taken into consideration.

3.3. Automatic identification of cells in FOV

As a specific fluorochrome for cellular nuclei, DAPI can label the nuclei, making the targets easy to be extracted from the background. In this experiment, a binarization process was used to separate the background and the targets. The single-wavelength image at 492 nm (Fig. 7(a)) was selected for the image processing due to the difference in grayscale level between background and targets was the biggest. Then, a threshold for the binarization was set for the separation of background and targets. If the grayscale value of a pixel in the FOV was higher than the threshold, its value would be set as 1 (targets); otherwise, its value would be set as 0 (background).

A connected-region algorithm was used to label different nuclei as different regions in the binary image (Fig. 7(b)). If most of the target pixels inside the border of a nucleus were labeled as cancerous by the SVM model, the corresponding cell will be identified as a cancer cell, and vice versa. With this method, cells can be precisely identified, even though there is a small number of pixels inside the border were incorrectly labeled. Figure 7(c) is a pseudo-color image for showing the identified result in the FOV, with the nuclei of cancer cells labeled in red and that of the normal nuclei labeled in green.

Biomedical Optics EXPRESS

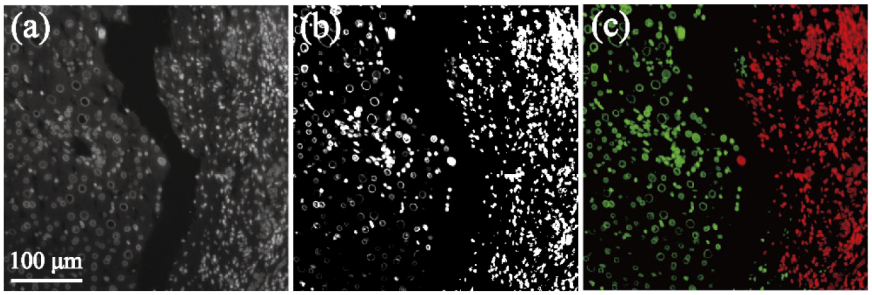

Fig. 7. Imaging processing for automatic identification of cells in FOV. (a) is the original single wavelength at 492 nm. (b) is the binarized image. (c) is the pseudo-color image of the identification result.

4. Conclusion

Given that the hyperspectral microscopy can obtain more information than the flow cytometry, it was exploited to examine the DAPI-stained hepatic carcinoma cells and normal hepatic cells firstly in this study. Harnessing the hyperspectral microscopy, we find that emissions from normal and cancer nuclei are different not only in the fluorescent intensity but also in the spectral shape. Further investigation showed the DAPI-DNA complex owns two emission centers and they react differently to the DNA content. Therefore, the difference in DNA content between normal and cancer nuclei leads to the difference in the intensity and the spectral shape of their fluorescence. These properties can be used to realize the precise identification of hepatic carcinoma cells and normal hepatic cells.

Funding

Key-Area Research and Development Program of Guangdong Province (2020B090922006); National Natural Science Foundation of China (61935010, 61975069); Guangdong Project of Science and Technology Grants (2018B030323017); Guangzhou science and technology project (201903010042, 201904010294).

Disclosures

The authors declare no conflicts of interest.

References

1. B. I. Tarnowski, F. G. Spinale, and J. H. Nicholson, "DAPI as a useful stain for nuclear quantitation," Biotech. Histochem. **66**(6), 296–302 (1991).
2. J. Kapuscinski, "DAPI: a DNA-specific fluorescent probe," Biotech. Histochem. **70**(5), 220–233 (1995).
3. W. Göhde, J. Schumann, and J. Zante, "The use of DAPI in pulse cytophotometry," Pulse cytophotometry **3**, 229–232 (1978).
4. M. Noirot, P. Barre, J. Louarn, C. Duperray, and S. Hamon, "Consequences of stoichiometric error on nuclear DNA content evaluation in Coffea liberica var. dewevrei using DAPI and propidium iodide," Ann. Bot. **89**(4), 385–389 (2002).
5. J. Wen, A. Krishan, and R. A. Thomas, "NASA/American Cancer Society high-resolution flow cytometry project–II. Effect of pH and DAPI concentration on dual parametric analysis of DNA/DAPI fluorescence and electronic nuclear volume," Cytometry: The Journal of the International Society for Analytical Cytology **43**(1), 12–15 (2001).
6. T. N. Siegel, D. R. Hekstra, and G. A. Cross, "Analysis of the Trypanosoma brucei cell cycle by quantitative DAPI imaging," Mol. Biochem. Parasitol. **160**(2), 171–174 (2008).
7. T. J. Pugh, "Circulating tumour DNA for detecting minimal residual disease in multiple myeloma," Semin. Hematol. **55**(1), 38–40 (2018).
8. Y. Wang, V. W. S. Liu, W. C. Xue, A. N. Y. Cheung, and H. Y. S. Ngan, "Association of decreased mitochondrial DNA content with ovarian cancer progression," Br. J. Cancer **95**(8), 1087–1091 (2006).

Biomedical Optics EXPRESS

9. B. I. Gerashchenko, K. Salmina, J. Eglitis, and J. Erenpreisa, "Probing breast cancer therapeutic responses by DNA content profiling," Int. J. Med. Biomed. Res. **5**(1), 47–57 (2019).
10. H. Isobe, H. Miyamoto, T. Shimizu, H. Haneda, M. Hashimoto, K. Inoue, S. Mizuno, and Y. Kawakami, "Prognostic and therapeutic significance of the flow cytometric nuclear DNA content in non-small cell lung cancer," Cancer **65**(6), 1391–1395 (1990).
11. C. Deprez, D. Vangansbeke, R. Fastrez, J. L. Pasteels, A. Verhest, and R. Kiss, "Nuclear DNA content, proliferation index, and nuclear size determination in normal and cirrhotic liver, and in benign and malignant primary and metastatic hepatic tumors," Am. J. Clin. Pathol. **99**(5), 558–565 (1993).
12. D. W. Hedley, C. A. Rugg, and R. D. Gelber, "Association of DNA index and S-phase fraction with prognosis of nodes positive early breast cancer," Cancer Res. **47**(17), 4729–4735 (1987).
13. E. Kho, B. Dashtbozorg, L. L. De Boer, K. K. Van de Vijver, H. J. Sterenborg, and T. J. Ruers, "Broadband hyperspectral imaging for breast tumor detection using spectral and spatial information," Biomed. Opt. Express **10**(9), 4496–4515 (2019).
14. M. Ishikawa, C. Okamoto, K. Shinoda, H. Komagata, C. Iwamoto, K. Ohuchida, M. Hashizume, A. Shimizu, and N. Kobayashi, "Detection of pancreatic tumor cell nuclei via a hyperspectral analysis of pathological slides based on stain spectra," Biomed. Opt. Express **10**(9), 4568–4588 (2019).
15. J. Unger, C. Hebisch, J. E. Phipps, J. L. Lagarto, H. Kim, M. A. Darrow, R. J. Bold, and L. Marcu, "Real-time diagnosis and visualization of tumor margins in excised breast specimens using fluorescence lifetime imaging and machine learning," Biomed. Opt. Express **11**(3), 1216 (2020).
16. S. Ortega, H. Fabelo, R. Camacho, M. De la Luz Plaza, R. G. M. Callicó, and Sarmiento, "Detecting brain tumor in pathological slides using hyperspectral imaging," Biomed. Opt. Express **9**(2), 818–831 (2018).
17. M. Halicek, J. D. Dormer, J. V. Little, A. Y. Chen, and B. Fei, "Tumor detection of the thyroid and salivary glands using hyperspectral imaging and deep learning," Biomed. Opt. Express **11**(3), 1383–1400 (2020).
18. Y. Chen, S. Zhu, S. Fu, Z. Li, F. Huang, H. Yin, and Z. Chen, "Classification of hyperspectral images for detection of hepatic carcinoma cells based on spectral–spatial features of nucleus," J. Innovative Opt. Health Sci., 2050002 (2019).
19. S. Zhu, K. Su, Y. Liu, H. Yin, Z. Li, F. Huang, and Y. Chen, "Identification of cancerous gastric cells based on common features extracted from hyperspectral microscopic images," Biomed. Opt. Express **6**(4), 1135–1145 (2015).
20. K. Erhardt, G. Auer, E. Björkholm, G. Forsslund, B. Moberger, C. Silfverswärd, G. Wicksell, and A. Zetterberg, "Prognostic significance of nuclear DNA content in serous ovarian tumors," Cancer Res. **44**(5), 2198–2202 (1984).
21. A. G. Fallenius, G. U. Auer, and S. A. Franzén, "Predictive value of nuclear DNA content in breast cancer in relation to clinical and morphologic factors. A retrospective study of 227 consecutive cases," Cancer **62**(3), 521–530 (1988).
22. S. Toikkanen, H. Joensuu, and P. Klemi, "The prognostic significance of nuclear DNA content in invasive breast cancer–a study with long-term follow-up," Br. Br. J. Cancer **60**(5), 693–700 (1989).
23. T. Ince, S. Kiranyaz, L. Eren, M. Askar, and M. Gabbouj, "Real-time motor fault detection by 1-D convolutional neural networks," IEEE Transactions on Industrial Electronics **63**(11), 7067–7075 (2016).